PHYSICAL SCIENCES

Oxygen activation on Ba-containing perovskite materials

Yue Zhu[1,2]†, Dongdong Liu[3,4]†, Huijuan Jing[1,2]†, Fei Zhang[1,2,3], Xiaoben Zhang[2,3], Shiqing Hu[1,2], Liming Zhang[1,2], Jingyi Wang[1,2], Lixiao Zhang[1,2], Wenhao Zhang[1,2], Bingjie Pang[1,4], Peng Zhang[1], Fengtao Fan[1,2,3], Jianping Xiao[1,2], Wei Liu[2,3], Xuefeng Zhu[1,2]*, Weishen Yang[1,2]*

Oxygen activation, including oxygen reduction reaction (ORR) and oxygen evolution reaction (OER), is at the heart of many important energy conversion processes. However, the activation mechanism of Ba-containing perovskite materials is still ambiguous, because of the complex four-electron transfer process on the gas-solid interfaces. Here, we directly observe that BaO and BaO_2 segregated on Ba-containing material surface participate in the oxygen activation process via the formation and decomposition of BaO_2. Tens of times of increase in catalytic activities was achieved by introducing barium oxides in the traditional perovskite and inert Au electrodes, indicating that barium oxides are critical for oxygen activation. We find that BaO and BaO_2 are more active than the B-site of perovskite for ORR and OER, respectively, and closely related to the high activity of Ba-containing perovskite.

INTRODUCTION

Oxygen exchange reactions, including oxygen reduction reaction (ORR) and oxygen evolution reaction (OER), occurring at gas-solid interfaces are vital to the process of energy conversion in metal-air batteries (*1*), solid oxide cells (SOCs) (*2*–*5*), water splitting (*6*), and catalytic membrane reactors (*7*). The activation mechanism of oxygen at gas-solid interfaces is still unclear, because the complex four-electron transfer process is related to various oxygen species, evolving with the material composition and structure, as well as the reaction conditions (*8*–*12*). Elucidating the oxygen activation mechanism is of great significance for the design and preparation of new materials with high activity for energy conversion devices. Although notable advances have been achieved in recent decades, a multitude of ambiguous relationships between researches of experiments and theory still need to be disclosed.

Transition metals, such as Mn, Fe, Co, and Ni, in the B-sites of perovskite-type oxides ($ABO_{3-\delta}$) are generally considered as active sites because both the mixed valence states of the transition metals and medium B—O bond length are favorable for oxygen activation (*12*–*18*). However, the segregation of alkaline earth elements, i.e., Ba, Sr, and Ca, in the A-sites of perovskites and double perovskites in an oxygen-enriched atmosphere has been widely reported (*19*–*26*). The degradation of electrode catalytic activity was even suggested to closely correlate to the segregation of alkaline earth elements on perovskite surfaces (*22*–*26*). The segregation tendency of alkaline earth elements is directly related to cationic size (*27*, *28*). Ba is easier to segregate on the perovskite surface compared to other alkaline-earth and lanthanide elements. We find an interesting phenomenon that perovskite-type materials containing Ba in A-sites have outstanding activity toward oxygen activation compared to materials with similar structures and compositions, as shown in fig. S1. Several studies indicated that the catalytic activity of perovskites can be markedly improved by introducing $BaCO_3$, although $BaCO_3$ was regarded as an inert matter toward oxygen exchange reactions (*29*, *30*). Therefore, the authentic character of A-site elements toward the oxygen activation process remains a debate, especially the role of Ba in the oxygen exchange reactions of Ba-containing materials.

Here, we disclose another mechanism of oxygen exchange reactions for Ba-containing materials where BaO/BaO_2 acts as active sites. $Ba_{0.5}Sr_{0.5}Co_{0.8}Fe_{0.2}O_{3-\delta}$ (BSCF), which is widely investigated in energy conversion processes, is chosen as a representative to explore the positive effect of Ba doping because of its high catalytic activity toward oxygen activation. Kinetic analysis shows that the oxygen exchange rates can be significantly improved by increasing the Ba content in $Ba_xSr_{1-x}Co_{0.8}Fe_{0.2}O_{3-\delta}$ (x = 0, 0.1, 0.3, 0.5, and 0.7). Nanoparticles and peroxide species are found on the surface of BSCF disks after being treated in the O_2-rich atmosphere at elevated temperature. The nanoparticles and peroxide species are further identified to be barium oxides by using an environmental transmission electron microscope (ETEM) under oxygen atmosphere at elevated temperatures. Strong evidence from electrochemical experiments shows that barium oxides and Ba-containing materials, which are prone to decomposition into barium oxides, have high catalytic activity toward oxygen activation. The high activity is related to the low-energy barriers of oxygen adsorption/dissociation and combination/desorption on BaO and BaO_2 at elevated temperatures, respectively, which is demonstrated by the results of density functional theory (DFT) calculations of oxygen activation on BaO/BaO_2 and B-site of BSCF. Therefore, BaO and BaO_2 segregated on the surface of Ba-containing perovskite have high activities toward ORR and OER, respectively.

RESULTS AND DISCUSSION

Oxygen exchange kinetics and microstructure variation of $Ba_xSr_{1-x}Co_{0.8}Fe_{0.2}O_{3-\delta}$

$Ba_xSr_{1-x}Co_{0.8}Fe_{0.2}O_{3-\delta}$ (x = 0, 0.1, 0.3, 0.5, and 0.7) materials were selected as examples to understand the effect of Ba doping on oxygen activation (*11*, *31*–*34*). The oxygen exchange coefficients under working steady states were obtained using a kinetic model [a brief introduction to the kinetic model and the permeation resistance constants

[1]State Key Laboratory of Catalysis, Dalian Institute of Chemical Physics, Chinese Academy of Sciences, 457 Zhongshan Road, Dalian 116023, China. [2]University of Chinese Academy of Sciences, Beijing 100039, China. [3]Dalian National Laboratory for Clean Energy, Dalian 116023, China. [4]Dalian University of Technology, 2 Linggong Road, Dalian 116024, China.
*Corresponding author. Email: zhuxf@dicp.ac.cn (X.Z.); yangws@dicp.ac.cn (W.Y.)
†These authors contributed equally to this work.

(fig. S2) are shown in the Supplementary Materials], and the results are shown in Fig. 1A. A small amount of Ba doping (mole percentage, 10%) can significantly improve both the ORR and OER oxygen exchange coefficients. With an increase in Ba content in $Ba_xSr_{1-x}Co_{0.8}Fe_{0.2}O_{3-\delta}$, interfacial exchange coefficients of both ORR and OER reach a maximum at a Ba doping amount of 0.5. This promotion effect of Ba doping becomes more obvious at lower temperatures. The interfacial exchange coefficients of ORR and OER of BSCF are about 2.0 and 2.6 times those of $SrCo_{0.8}Fe_{0.2}O_{3-\delta}$ (SCF) at 820°C, respectively. Changes in the valence states of transition metals and oxygen vacancy concentration are usually inferred as being responsible for such improvements. However, the average valence state of B-site cations and the oxygen vacancy concentration remain almost unchanged for different Ba doping amounts, as shown in tables S1 and S2. Thus, it is worth thinking about why the slight change of Ba amount in A-sites can produce such a remarkable improvement in the catalytic activity. We suspect that Ba in the A-sites of the perovskite may play an important but yet undiscovered role in oxygen exchange reactions. Further study should be carried out to investigate whether species or sites that contain Ba act as the active sites for oxygen exchange reactions.

Four polished BSCF disks were treated at 850°C in flowing O_2 for 0, 10, 20, and 30 hours, respectively. No nanoparticles were observed on the original surface of the BSCF disk before treatment, while many nanoparticles appear on the surfaces after the treatment (Fig. 1B), and the number increases with time. The precipitation of nanoparticles was also observed on the surfaces of other Ba-containing mixed ionic-electronic conducting (MIEC) materials after treatment in air at elevated temperatures, such as $Ba_{0.7}Sr_{0.3}Co_{0.8}Fe_{0.2}O_{3-\delta}$ and $BaCe_{0.1}Fe_{0.9}O_{3-\delta}$ (fig. S3, A and B, respectively), but was not found on Ba-free MIEC materials annealing under similar conditions, such as $La_{0.6}Sr_{0.4}Co_{0.2}Fe_{0.8}O_{3-\delta}$ and $SrFeO_{3-\delta}$ (fig. S3, C and D, respectively) and SCF (fig. S4). Thus, nanoparticles prefer to precipitate on the surface of Ba-containing MIEC materials. The characteristic Raman band at 860 cm^{-1}, which is assigned to the peroxide species O_2^{2-}, was found in all the treated BSCF samples (Fig. 1C). BaO_2 cannot be excluded on the surface when other bands at 902, 930, and 986 cm^{-1} are taken into consideration (table S3). A preliminary study was carried out on the BSCF powder using ETEM (Fig. 1D). No apparent change was observed until the temperature was increased to 650°C. However, the morphology of the particles changed vigorously when the temperature was further raised to 800°C, where particles with sizes larger than 100 nm emerged, as seen in the top right corner of Fig. 1D. Ba and O are the major elements in this area, while Sr, Co, and Fe are almost negligible (fig. S5). Thus, the precipitation of barium oxides from BSCF occurs in O_2-rich atmospheres at elevated temperatures.

Microstructure and composition of segregated nanoparticles

The evolutionary process of microstructure and composition reconstruction on the BSCF surface was observed in real time using ETEM in oxygen atmosphere to help provide insights into the segregation mechanism of nanoparticles. Specifically, a thin BSCF slice (Fig. 2A) was fabricated through cutting a lamella from the bulk

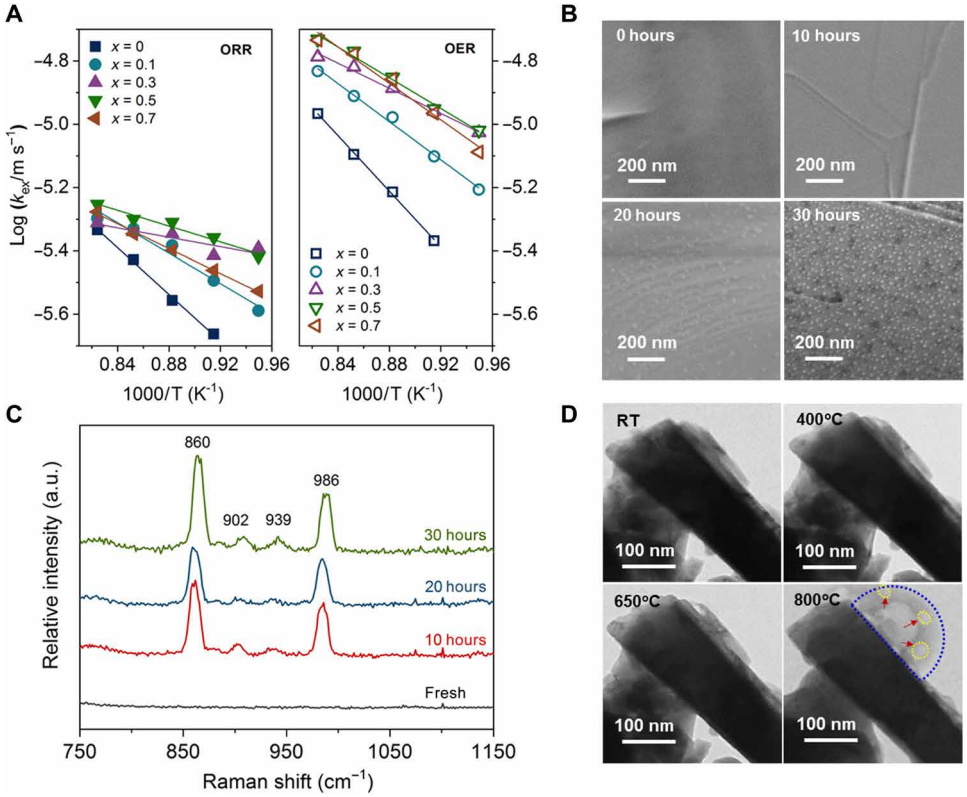

Fig. 1. Oxygen exchange kinetics and microstructure variation of Ba-containing perovskite oxides. (**A**) Dependence of oxygen exchange coefficients on Ba doping in $Ba_xSr_{1-x}Co_{0.8}Fe_{0.2}O_{3-\delta}$ (x = 0, 0.1, 0.3, 0.5, and 0.7). (**B**) Scanning electron microscopy (SEM) images and (**C**) ultraviolet (UV)–Raman spectra of $Ba_{0.5}Sr_{0.5}Co_{0.8}Fe_{0.2}O_{3-\delta}$ disks calcined at 850°C in O_2 for 0, 10, 20, and 30 hours. (**D**) The morphology variation of $Ba_{0.5}Sr_{0.5}Co_{0.8}Fe_{0.2}O_{3-\delta}$ powder with temperature in O_2 (8.84 mbar). RT, room temperature; a.u., arbitrary units.

BSCF sample and then transferred onto a microelectromechanical system–based heating reactor for in situ oxidation using the focused ion beam scanning electron microscopy (FIB-SEM) technology. The sample was in single crystal with an exposed (110) surface (Fig. 2B), and all the compositional elements were distributed uniformly over the entire BSCF slice (fig. S6), suggesting a homogeneous perovskite phase of the substrate. When heating this fresh sample under a 6-mbar O_2 atmosphere, oxidation triggers gradual growth of small nanoparticles on the slice surface. These nanoparticles tend to grow quickly as the temperature was increased to near 800°C (fig. S7). Benefiting of the reaction environment loading as during the microscopy observation, the above process was unambiguously witnessed as demonstrated in movie S1. Further increasing the reaction temperature to 900°C for 20 min, its surface became studded with pyramidal-shaped nanoparticles, which was evidenced by elemental *z*-number–related contrast distribution in the high-angle annular dark-field (HAADF) image (Fig. 2C).

The composition of precipitated nanoparticles on the BSCF substrate surface was analyzed using the techniques of scanning transmission electron microscopy (STEM) coupled with electron energy-loss spectroscopy (EELS). As shown in Fig. 2D, the nanoparticles are mainly composed of Ba and O in the absence of cobalt and iron counterparts. The above facts imply that the reaction-induced nanoparticle belongs to the Ba-containing oxides, given the correlated distribution of oxygen and barium elements. Moreover, high-resolution TEM imaging (Fig. 2, E to G) of three independent particles along two zone axes proves that these precipitated nanoparticles are in distinctive BaO_2 phase (*I*4/*mmm*), which directly confirm the existence of BaO_2 phase during the oxidation reaction–induced surface reconstruction of BSCF perovskite. Additional evidence also disclosed that under oxidation conditions, the segregation of barium oxides could occur on the BSCF particle surface at lower gas pressures and temperatures (figs. S8 to S13 and movies S2 to S5). Particles, including $BaO_{1.3}$ and BaO in sizes of 5 to 20 nm, were found in the segregation area (fig. S9 and table S4). BaO_2 decomposition and oxygen evolution were also captured as the oxygen pressure decreased, as revealed by the appearance of bubbles in the segregation area (Fig. 1D and figs. S9 and S12). During ETEM measurement, the segregation of barium oxides tended to be steady, and the nanoparticles did not grow further at a certain temperature in O_2, while the collapse of perovskite structure was not observed. There will be a gradient of Ba content in the bulk near the perovskite surface and some defects on the lattice position of Ba. However, if too much Ba segregated from the bulk, then BSCF may not keep the perovskite structure.

Catalytic activity of composite electrodes containing barium oxides

BaO was used as an adsorbent for air separation at middle-elevated temperatures before the emergence of cryogenic distillation technology, because BaO can easily adsorb oxygen from the air to form

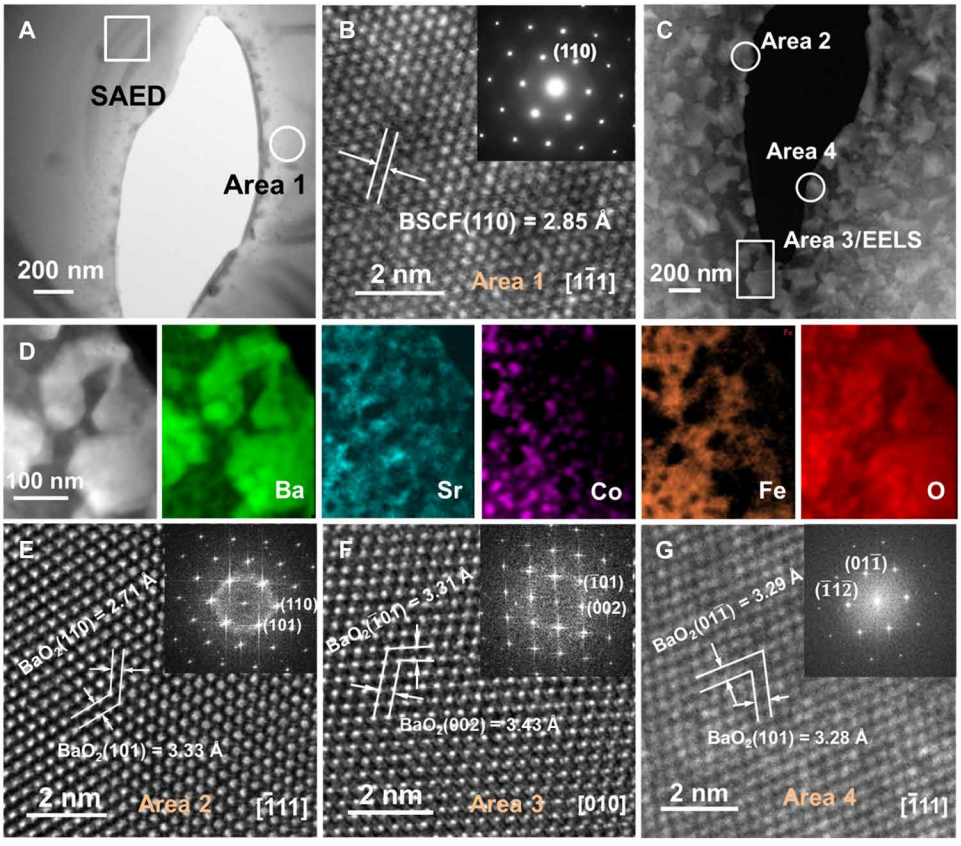

Fig. 2. Structure analysis of the in situ segregated precipitate on BSCF in ETEM. (**A**) Low-magnification transmission electron microscope (TEM) image of BSCF before oxidation. (**B**) High-resolution TEM images and selected area electron diffraction (SAED) from the area 1 and SAED marked in (A), respectively. (**C**) HAADF-STEM image after in situ oxidization at 900°C for 20 min. (**D**) Composition analysis of selected area 3 in (C) through STEM-EELS mapping. (**E** to **G**) The microstructure of three different precipitates from marked areas 2, 3, and 4, respectively.

BaO_2, which can then rapidly release O_2 in an O_2-poor atmosphere (*35*, *36*). Adsorption and dissociation of molecular O_2 and the transport of oxygen species are the possible rate-determining steps in the process of oxygen activation (table S5). Thus, we inferred that the segregated barium oxides at the surface will greatly improve the catalytic activity of MIEC materials toward oxygen exchange reactions. To confirm the above hypothesis, we prepared symmetric cells of BaO-Au|SDC|BaO-Au to determine the polarization resistance as a function of BaO content. The preparation conditions, morphologies, and structures of the symmetric cells are shown in table S6 and figs. S14 and S15, respectively. The polarization resistance of the 10% BaO-Au composite electrode is far lower than that of the Au electrode (Fig. 3A), and it decreases with an increase in BaO content. The activity difference between the Au and BaO-Au composite electrodes becomes much larger at low temperatures because the activation energy of the latter is only approximately half that of the former (Fig. 3B). This result indicates that barium oxides indeed exhibit high catalytic activity toward oxygen activation. Meanwhile, $BaCO_3$-Au and $BaSO_4$-Au composite electrodes were tested in flowing air at 800°C (Fig. 3C). Significantly improved catalytic activity of $BaCO_3$ was observed, indicated by the decrease in polarization resistance. The polarization resistance decreased with an increase in duration time, because $BaCO_3$ could further partially decompose into barium oxides in flowing synthetic air at 800°C (figs. S16 and S17). It also offers a reasonable explanation that the catalytic activity of perovskites can be markedly improved by introducing $BaCO_3$ (*29*, *30*). For many works, barium oxides were hard to observe, because samples were prepared under air before characterizations or observed under ambient temperature and pressure through common equipment. The practicality of materials containing Ba for ORR is still questionable now when ambient air is used as the feed gas, because the decomposition of $BaCO_3$ is inhibited under an atmosphere containing CO_2. However, the barium oxides segregated from the bulk of Ba-containing materials or formed from the partial decomposition of $BaCO_3$ can remain stable in some practical applications without CO_2, for instance, as the OER catalyst on the permeation side of MIEC membranes for oxygen separation (*37*) and as the anode of solid oxide electrolytic cells (*38*, *39*). Different from $BaCO_3$, $BaSO_4$ shows lower activity toward oxygen exchange reactions because it cannot decompose into barium oxides in synthetic air at 800°C (fig. S18). The catalytic activities of composite electrodes containing other alkaline earth and lanthanide oxides are far lower than those of the BaO-Au composited electrodes (fig. S19), indicating that high catalytic activity is unique for BaO among these A-site elements in MIEC perovskite oxides.

Thus, promoting the formation of barium oxides on the surface of Ba-containing MIEC materials or adding BaO to electronic conductors to form a composite material is an effective strategy to accelerate oxygen exchange reactions. $(La_{0.75}Sr_{0.25})_{0.95}MnO_{3-\delta}$ (LSM), as a classical electrode, has been well studied in SOCs because of its high electron conductivity and stability. Its catalytic activity was significantly improved after a small amount of $Ba(OH)_2$ solution was injected into as-sintered LSM electrodes (Fig. 3D). BaO is the main active site for oxygen activation in the composite electrode because $Ba(OH)_2$ decomposes into BaO when the temperature is higher than 600°C (figs. S20 and S21). Meanwhile, the oxygen exchange activity

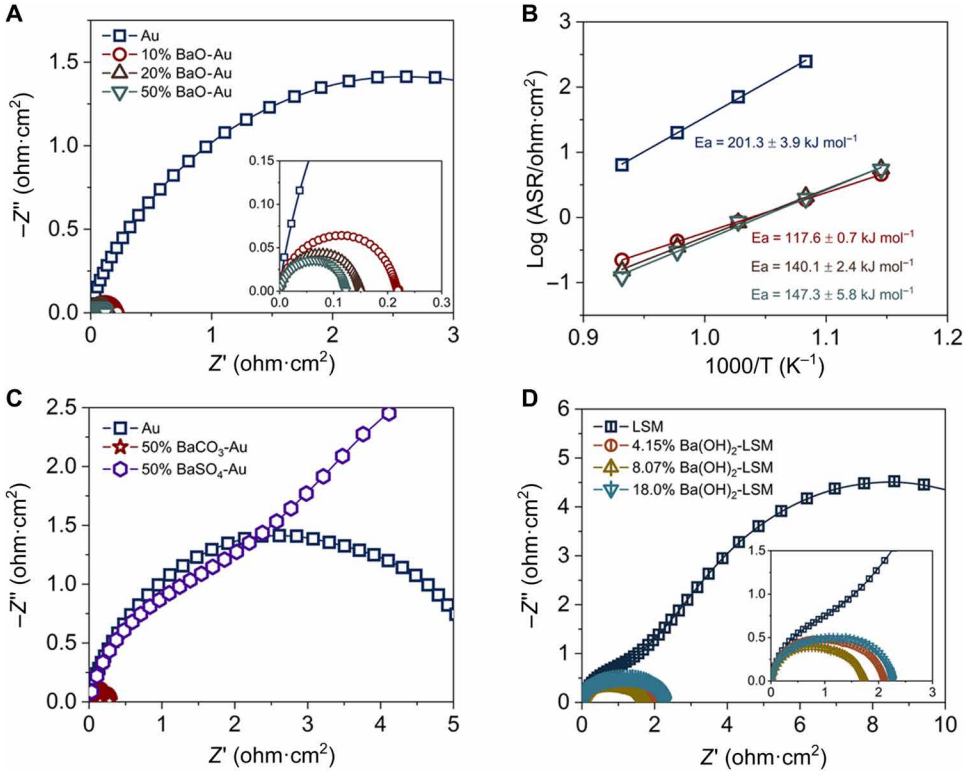

Fig. 3. Experiments of barium oxides for oxygen activation. (**A**) The electrochemical impedance spectra (EIS) (800°C) and (**B**) activation energies of BaO-Au|SDC|BaO-Au symmetric cells with different BaO content. ASR, area specific resistance. (**C**) The EIS of 50% $BaCO_3$/$BaSO_4$-Au|SDC|50% $BaCO_3$/$BaSO_4$-Au (800°C) and (**D**) LSM-$Ba(OH)_2$|SDC|LSM-$Ba(OH)_2$ (700°C) symmetric cells in air.

improved obviously after a small amount of $Ba(OH)_2$ solution was injected into the Au electrode (fig. S22).

DFT calculations of ORR and OER

On the basis of the experimental characterizations, BaO(111) and (100) as well as BSCF(001) and (110) were chosen with DFT calculation to compare the ORR activity, while the BaO_2(101) and (110) facets and the same BSCF facets were used to explore the OER performance. As shown in Fig. 4A and figs. S23 and S24, for the BSCF system, O_2 dissociations on BSCF(110) and (001) are similar with barriers of ~1.2 eV, although BSCF(110) favors O_2 adsorption by 0.65 eV than BSCF(001). However, BaO(111) exhibits an enhanced O_2 activation with a barrier of 0.17 eV with respect to BaO(100) surface (1.35 eV). This indicates that the BaO(111) surface is more active than the BaO(100) and BSCF surfaces, serving as active sites for efficient O_2 dissociation. On the other hand, the BaO_2(110) and (101) surfaces show similar lower barriers (1.03 and 1.05 eV, respectively) for O_2 evolution compared to both BSCF(110) (1.44 eV)

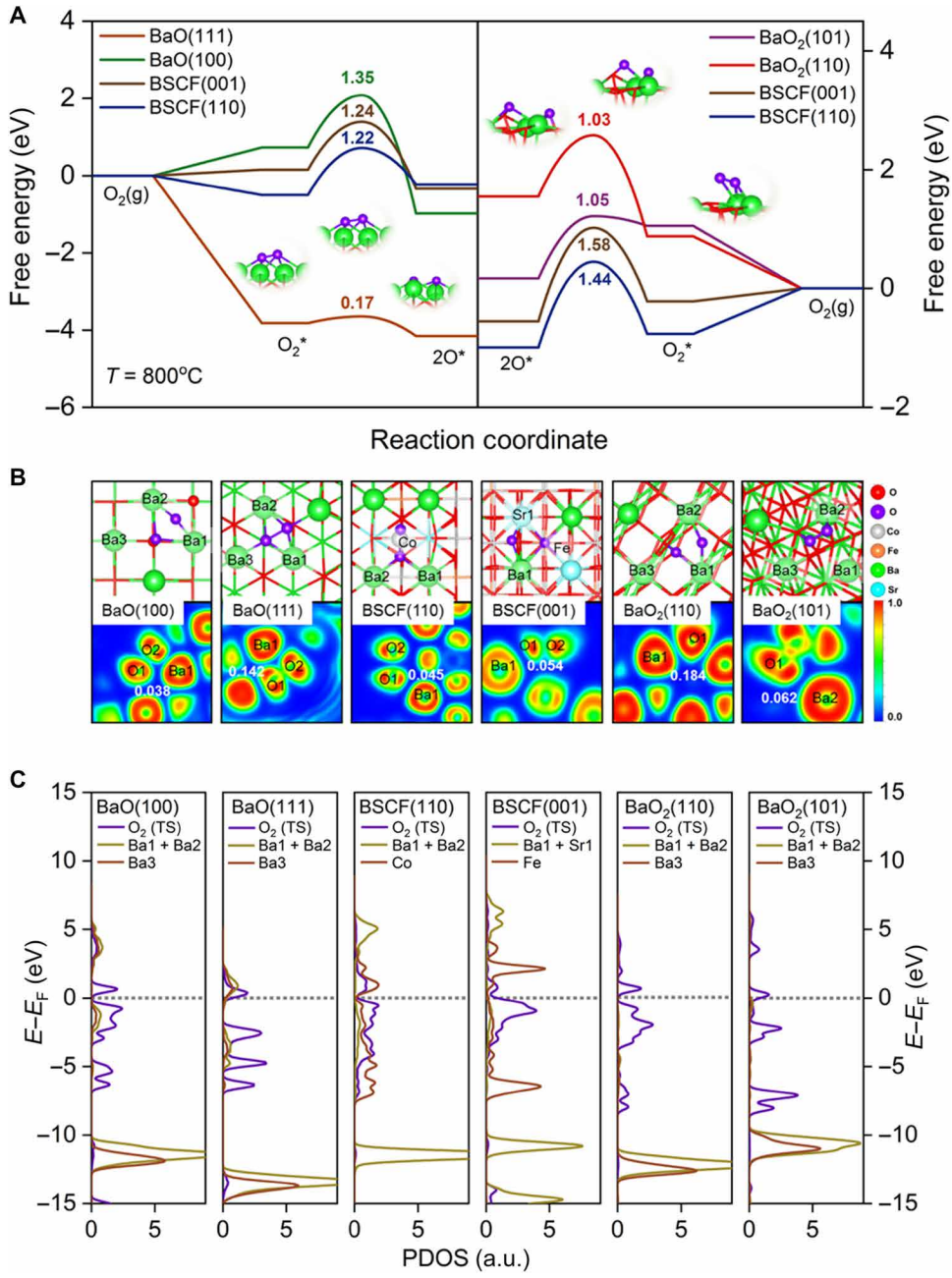

Fig. 4. DFT calculations of barium oxide and barium dioxide for ORR and OER. (**A**) Gibbs free energy (800°C) diagram for O_2 dissociation (left) and O_2 formation (right) on the four surfaces: BSCF(110) and (001) facets and BaO(100) and (111) facets as well as BSCF(110) and (001) facets and BaO_2(101) and (110) facets. (**B**) Corresponding atomic configurations (top view) and electron localization function (ELF) of the key O-Ba pairs for the TS. For clarity, the atoms are numbered, and ELF values are inserted. (**C**) Projected density of states (PDOS) of the key atoms [shown in (B)] involved in the TS (the dotted gray line marks the Fermi level).

and BSCF(001) (1.58 eV), which indicates the high activity on BaO_2 surfaces. Therefore, we deduce that BaO and BaO_2 have high activities for O_2 dissociation and O_2 evolution, respectively, in comparison to the BSCF, which is consistent with the experimentally electrochemical evaluation of composite electrodes that BaO/BaO_2 can improve oxygen exchange activity.

According to the transition states (TSs) in Fig. 4B, BSCF(110) and (001) provided an active ensemble composed of Ba1, Ba2 (or Sr1), and Co (or Fe) atoms, whereas Ba1, Ba2, and Ba3 play roles in O_2 activation on BaO and in O_2 evolution on BaO_2. Hybridization of the O_2 (TS) and active sites can qualitatively reflect the stability of bonding. In Fig. 4C, the projected density of states (PDOS) of O_2 (TS) for BaO(111) and BaO_2(110) downshifts versus other surfaces, indicating more hybridization between oxygen and surface. The electron localization function (ELF) analysis in Fig. 4B also demonstrates that the interactions are the strongest between O_2 (TS) and the surfaces of BaO(111) and BaO_2(110), boosting both dissociation and O_2 evolution. Intrinsically, BaO(111) is a polar surface with the Taker type 3 structure (*40*), which exposes a threefold coordinated Ba_{3c} with higher activity than those of Ba_{5c} on BaO(100) and Ba_{6c} (also Co_{4c} or Fe_{5c}) on the BSCF surfaces. It is noted that the O—O bond length on BaO(100) after O_2 dissociation is 1.49 Å, close to that (1.48 Å) in BaO_2 (fig. S25) (*41*). The surface (cleavage) energy of BaO(111) is 0.53 eV/Å^2, compared to 0.07 eV/Å^2 for BaO(100). The resulting reactive oxygen atoms generated on BaO(111) can easily migrate to BaO(100), which is able to drive peroxide formation. Moreover, the O_2 evolution on BaO_2 is more facile than on BSCF.

From the aforementioned results, we can deduce that the mechanism of oxygen exchange reactions of Ba-containing MIEC materials has another route different from others, as shown in fig. S26. Ba first segregates from the bulk to the surface to form BaO under an oxygen-enriched atmosphere at elevated temperature. Element segregation has been widely investigated. The size mismatch between the host and the dopant and cationic defects in the bulk would induce the segregation of alkaline-earth metals in perovskite oxides (*20*, *42*, *43*). Ba is easier to segregation than Sr in BSCF because of the larger cation radius and the formation of BaO_2 in O_2-containing atmosphere (*20*, *28*). Then, BaO reacts with O_2 to form BaO_2 through inner electron transfer. Oxygen species transfer via BaO_2 to the surface of the MIEC material and then combine with oxygen vacancies and electrons from the MIEC material. Meanwhile, the resultant BaO participates in the next cycle. Furthermore, the dissociation of BaO_2 to produce O_2 was proven to be more facile than the O_2 evolution on BSCF. Thus, BaO and BaO_2 are the active sites for ORR and OER, respectively.

MATERIALS AND METHODS

Sample preparation and oxygen exchange kinetics analysis

The $Ba_xSr_{1-x}Co_{0.8}Fe_{0.2}O_{3-\delta}$ (x = 0, 0.1, 0.3, 0.5, and 0.7) powders were synthesized via sol-gel methods. Green disks of the five materials were obtained through pressing the powders at appropriate pressures in a stainless steel mold. The green disks were sintered at 1120° to 1200°C for 3 hours in a muffle furnace to obtain the dense membranes. All the disks were polished by 500-mesh SiC papers to 1.0 mm. After sealing with the silver rings at 961°C, the temperature was decreased to the target temperatures for the measurement. Synthetic air (150 ml min^{-1}) made of O_2 and N_2 with appropriate ratios was used as the feed gas. He was used as the sweeping gas. The composition of the effluent gas was analyzed by a gas chromatography instrument (Agilent 6890) equipped with a thermal conductivity detector. Oxygen permeation fluxes through these MIEC disks were calculated on the basis of the flow rates of sweeping gas and the oxygen concentration in the effluents. The oxygen exchange kinetics was obtained by using an oxygen permeation model at steady states. A brief introduction of the kinetic model and data analysis are shown in the Supplementary Materials.

SEM and ultraviolet-Raman spectroscopy characterizations

The dense as-prepared BSCF and SCF disks were polished by 2000-mesh SiC papers. The polished samples were calcined at 850°C in O_2 for 0, 10, 20, and 30 hours, respectively. Scanning electron microscope (JSM 7900F) measurement was performed to observe the microstructure and morphology after the treatment. After SEM characterization, the treated BSCF disks were measured by the ultraviolet (UV)–Raman spectra. UV-Raman spectra were collected using a homebuilt spectrometer. The system was composed of a 325-nm semiconductor laser (Changchun New Industries Optoelectronics Technology Co.), a 25-mm-diameter off-axis parabolic mirror (Edmund Optics Co.) as the light-collecting element, an edge filter (Semrock Co.) to filter Rayleigh scattered light, a spectrograph (Shamrock 500), and a UV charge-coupled device camera (Newton 920) produced by Andor. All spectra were calibrated by placing the main Raman peak of polytetrafluoroethylene and highly oriented pyrolytic graphite. The laser power at the sample was kept below 2 mW to prevent burning effects.

ETEM characterization and elements analysis

In situ TEM experiments were carried out on both Titan Themis G3 (Titan-ETEM, Thermo Fisher Scientific Company) and Hitachi HF5000 environmental scanning transmission electron microscope (HF5000-ESTEM, Hitachi). The Titan-ETEM works at 300 kV with a spherical-aberration (Cs) corrector for parallel imaging (CEOS GmbH) and measured resolution of better than 1.0 Å. The Titan-ETEM is equipped with High-Speed STEM EELS (777.U1 + 777.U2), GIF Quantum ER basic package (965), and DualEELS (963.U3). Injecting O_2 (8.84 mbar/6 mbar) into the ETEM chamber with a self-developed gas system, the heating temperature increases and decreases to the target temperatures at a rate of 50°C s^{-1} by a DENS heating holder. The TEM images and movie series of the powder sample observed on Titan-ETEM were recorded by a Gatan OneView camera. In situ STEM was also performed by Titan-ETEM. Images were acquired using HAADF and bright-field detectors. The movie of the FIB sample was combined by a series of STEM images. For the HAADF imaging, a condenser aperture of 50 μm and a 195-mm camera length were used, obtaining the convergence angle of ~19.6 mrad and collection angle range of 40 to 200 mrad. STEM imaging was adopted to get high-quality EELS data. We set a camera length of 60 mm and a condenser aperture of 70 μm. EELS spectra were acquired in Dual EELS mode allowing for the precise calibration of the peak. EELS mapping was acquired with an energy dispersion of 1 eV/pixel and acquisition time of 0.1 s/pixel. EELS datasets were processed by using Digital Micrograph.

The in situ STEM experiments were performed on the HF5000-ETEM that works at 200 kV in the Hitachi FE-S/TEM system with a resolution of better than 1.0 Å. The energy-dispersive x-ray spectroscopy elemental mapping results were conducted at symmetrically opposed, dual 100-mm^2 EDX* detectors ("Symmetrical Dual SDD*")

equipped on the HF5000 microscope. The STEM images were acquired under HADDF mode with gas (6 Pa) being inlet via a gas nozzle toward the sample location. The movies were recorded on a build-in module.

Fabrication of symmetric cells and electrochemical testing

Dense $Sm_{0.2}Ce_{0.8}O_{2-\delta}$ (SDC) disks with thicknesses of 700 and 500 μm were used as electrolytes. Au powder with high purity (99.9%) was mixed with BaO powder (99.9%; Sigma-Aldrich) with mass ratios of 1:1 (50% BaO), 4:1 (20% BaO), and 9:1 (10% BaO), respectively, to obtain the electrode slurries. All powders were well mixed in the terpilenol solution containing ethyl cellulose. LSM powder was well mixed with the terpilenol solution containing ethyl cellulose. Then, the electrode slurries were painted onto both surfaces of the SDC substrate. Four symmetric cells, *w*% BaO-Au|SDC|*w*% BaO-Au (*w* = 0, 10, 20, and 50), were sintered at 850°C for 2 hours. Au paste was printed on the surface of the electrodes for current collection. Four symmetric cells, LSM|SDC|LSM, were sintered at 1100°C for 2 hours. $Ba(OH)_2$ solution (10, 20, and 50 μl) (0.0910 M) was injected into the LSM electrodes of the symmetric cells. The symmetric cells, Au|SDC|Au, were sintered at 900°C for 2 hours in a muffle furnace. Vacuum impregnation was applied to inject $Ba(OH)_2$ (0.045 M) solution into the small pores of Au electrode for 5 min. The fabricated symmetric cells were evaluated on a homemade test station with two-electrode electrochemical measurement. Both sides of the cell were fed with synthetic air (O_2:N_2 = 21:79) with a flow rate of 50 ml min^{-1} during heating and testing to eliminate the influence of CO_2 and other possible impurities in the environment. The heating rate was 2.67°C min^{-1}. All the measurements were started until the temperature was held at target temperatures for 30 min in flowing synthetic air with a flow rate of 50 ml min^{-1}. The electrochemical impedance spectra were carried out using an electrochemical workstation (a Solartron 1287 electrochemical interface and a Solartron 1260 frequency response analyzer).

Computational methods and models

DFT calculations have been performed using the Vienna Ab initio Simulation Package code (*44*, *45*) with the implemented projector augmented-wave method (*46*). The generalized gradient approximation in the Perdew-Burke-Ernzerhof form (*47*) was used to describe electronic exchange and correlation. A plane-wave basis set was specified with a cutoff of 400 eV. In addition, the van der Waals dispersion forces were corrected using the zero damping DFT-D3 method of Grimme (*48*). An on-site Hubbard term U_{eff} was added to address the open-shell *d*-electrons, which are 4.0 eV for Fe and 3.3 eV for Co (*49*). The energies and residual forces were converged to 10^{-6} eV and 0.02 eV $Å^{-1}$, respectively.

According to the characterizations by x-ray diffraction (XRD) and TEM, the crystal structures are referenced to BaO ($Fm\bar{3}m$, no. 225), BaO_2 ($I4/mmm$, no. 139), and $SrCoO_3$ ($Pm\bar{3}m$, no. 221), where the Ba_4O_4, the Ba_2O_4, and the $SrCoO_3$-derived $Ba_4Sr_4Co_6Fe_2O_{12}$ (fig. S23C) serve as the unit cells to simulate the experimental BaO, BaO_2, and BSCF structures. On the basis of the experimental characterization, the (111) and (100) facets of BaO, the (101) and (110) facets of BaO_2, and the (001) and (110) facets of BSCF were chosen as the prototypes (fig. S23). The optimized lattice constants are a = 5.53 Å for BaO, a = 3.80 Å and c = 6.86 Å for BaO_2, and a = 7.88 Å for BSCF. A slab with five layers was used to mimic the BSCF(110) and BSCF(001). The slab thicknesses are five and four atomic layers, respectively, for BaO(111) and (100). In addition, the slab thicknesses are nine and four atomic layers, respectively, for BaO_2(101) and (110). For irreducible Brillouin zone sampling, a Monkhorst-Pack k-point grid of 3 × 3 × 3 was adopted for BSCF bulk, 4 × 4 × 4 for BaO and BaO_2 bulk, and 2 × 2 × 1 for slab models. The vacuum distance was about 15 Å between slabs to avoid the undesired interaction.

Energy levels of the states were corrected to Gibbs free energies by the formula

$$G(T) = E_{elec} + \mathrm{ZPE} - TS$$

where E_{elec} is the electronic energy calculated by DFT at 0 K, ZPE is the zero point energy, S is the entropy, and system temperature T is 1073 K. For adsorbed species, the last two items were obtained by vibrational frequency calculations via standard methods (*50*). The adsorption energies of O_2 on the four surfaces at 0 K and the ZPE-$T\Delta S$ values at 1073 K are listed in table S7.

SUPPLEMENTARY MATERIALS

Supplementary material for this article is available at https://science.org/doi/10.1126/sciadv.abn4072

REFERENCES AND NOTES

1. Z. Lyu, Y. Zhou, W. Dai, X. Cui, M. Lai, F. Huo, W. Huang, Z. Hu, W. Chen, Recent advances in understanding of the mechanism and control of Li_2O_2 formation in aprotic Li-O_2 batteries. *Chem. Soc. Rev.* **46**, 6046–6072 (2017).
2. L. Yang, S. Wang, K. Blinn, M. Liu, Z. Liu, Z. Cheng, M. Liu, Enhanced sulfur and coking tolerance of a mixed ion conductor for SOFCs: $BaZr_{0.1}Ce_{0.7}Y_{0.2-x}Yb_xO_{3-\delta}$. *Science* **326**, 126–129 (2009).
3. C. Duan, R. J. Kee, H. Zhu, C. Karakaya, Y. Chen, S. Ricote, A. Jarry, E. J. Crumlin, D. Hook, R. Braun, N. P. Sullivan, R. O'Hayre, Highly durable, coking and sulfur tolerant, fuel-flexible protonic ceramic fuel cells. *Nature* **557**, 217–222 (2018).
4. A. Hauch, R. Küngas, P. Blennow, A. B. Hansen, J. B. Hansen, B. V. Mathiesen, M. B. Mogensen, Recent advances in solid oxide cell technology for electrolysis. *Science* **370**, eaba6118 (2020).
5. M. H. D. Othman, N. Droushiotis, Z. Wu, G. Kelsall, K. Li, High-performance, anode-supported, microtubular SOFC prepared from single-step-fabricated, dual-layer hollow fibers. *Adv. Mater.* **23**, 2480–2483 (2011).
6. Y. Zhu, W. Zhou, Y. Zhong, Y. Bu, X. Chen, Q. Zhong, M. Liu, Z. Shao, A perovskite nanorod as bifunctional electrocatalyst for overall water splitting. *Adv. Energy Mater.* **7**, 1602122 (2017).
7. L. Jia, G. He, Y. Zhang, J. Caro, H. Jiang, Hydrogen purification through a highly sTab. dual-phase oxygen-permeable membrane. *Angew. Chem. Int. Ed.* **60**, 5204–5208 (2021).
8. R. Ma, G. Lin, Y. Zhou, Q. Liu, T. Zhang, G. Shan, M. Yang, J. Wang, A review of oxygen reduction mechanisms for metal-free carbon-based electrocatalysts. *NPJ Comput. Mater.* **5**, 78 (2019).
9. N. T. Suen, S. F. Hung, Q. Quan, N. Zhang, Y. J. Xu, H. M. Chen, Electrocatalysis for the oxygen evolution reaction: Recent development and future perspectives. *Chem. Soc. Rev.* **46**, 337–365 (2017).
10. W. T. Hong, M. Risch, K. A. Stoerzinger, A. Grimaud, J. Suntivichb, Y. Shao-Horn, Toward the rational design of non-precious transition metal oxides for oxygen electrocatalysis. *Energy Environ. Sci.* **8**, 1404–1427 (2015).
11. J. Suntivich, K. J. May, H. A. Gasteiger, J. B. Goodenough, Y. Shao-Horn, A perovskite oxide optimized for oxygen evolution catalysis from molecular orbital principles. *Science* **334**, 1383–1385 (2011).
12. Y. Zhu, W. Zhou, Z. Shao, Perovskite/carbon composites: Applications in oxygen electrocatalysis. *Small* **13**, 1603793 (2017).
13. G. M. Rupp, A. K. Opitz, A. Nenning, A. Limbeck, J. Fleig, Real-time impedance monitoring of oxygen reduction during surface modification of thin film cathodes. *Nat. Mater.* **16**, 640–645 (2017).
14. G. M. Rupp, H. Tellez, J. Druce, A. Limbeck, T. Ishihara, J. Kilner, J. Fleig, Surface chemistry of $La_{0.6}Sr_{0.4}CoO_{3-\delta}$ thin films and its impact on the oxygen surface exchange resistance. *J. Mater. Chem. A* **3**, 22759–22769 (2015).
15. Y. Sun, Z. Liu, W. Zhang, X. Chu, Y. Cong, K. Huang, S. Feng, Unfolding B—O—B bonds for an enhanced ORR performance in ABO_3-type perovskites. *Small* **15**, e1803513 (2019).

16. J. Suntivich, H. A. Gasteiger, N. Yabuuchi, H. Nakanishi, J. B. Goodenough, Y. Shao-Horn, Design principles for oxygen-reduction activity on perovskite oxide catalysts for fuel cells and metal–air batteries. *Nat. Chem.* **3**, 546–550 (2011).
17. D. Chen, C. Chen, Z. M. Baiyee, Z. Shao, F. Ciucci, Nonstoichiometric oxides as low-cost and highly-efficient oxygen reduction/evolution catalysts for low-temperature electrochemical devices. *Chem. Rev.* **115**, 9869–9921 (2015).
18. Y. L. Huang, C. Pellegrinelli, E. D. Wachsman, Oxygen dissociation kinetics of concurrent heterogeneous reactions on metal oxides. *ACS Catal.* **7**, 5766–5772 (2017).
19. B. Wei, M. Schroeder, M. Martin, Surface cation segregation and chromium deposition on the double-perovskite oxide $PrBaCo_2O_{5+\delta}$. *ACS Appl. Mater. Interfaces* **10**, 8621–8629 (2018).
20. Y. Li, W. Zhang, Y. Zheng, J. Chen, B. Yu, Y. Chen, M. Liu, Controlling cation segregation in perovskite-based electrodes for high electro-catalytic activity and durability. *Chem. Soc. Rev.* **46**, 6345–6378 (2017).
21. S. P. Jiang, Activation, microstructure, and polarization of solid oxide fuel cell cathodes. *J. Solid State Electrochem.* **11**, 93–102 (2006).
22. W. Jung, H. L. Tuller, Investigation of surface Sr segregation in model thin film solid oxidefuel cell perovskite electrodes. *Energy Environ. Sci.* **5**, 5370–5378 (2012).
23. Y. Tian, S. He, Y. Liu, C. Yang, R. Yang, Y. Li, X. Wang, W. Li, B. Chi, J. Pu, Comprehensive understanding of alkaline-earth elements effects on electrocatalytic activity and stability of $LaFe_{0.8}Ni_{0.2}O_3$ electrode for high-temperature CO_2 electrolysis. *J. CO2 Util.* **53**, 101727 (2021).
24. J. Druce, H. Tellez, M. Burriel, M. D. Sharp, L. J. Fawcett, S. N. Cook, D. S. McPhail, T. Ishihara, H. H. Brongersmac, J. A. Kilner, Surface termination and subsurface restructuring of perovskite-based solid oxide electrode materials. *Energy Environ. Sci.* **7**, 3593–3599 (2014).
25. L. Zhu, B. Wei, Z. Wang, K. Chen, H. Zhang, Y. Zhang, X. Huang, Z. Lv, Electrochemically driven deactivation and recovery in $PrBaCo_2O_{5+\delta}$ oxygen electrodes for reversible solid oxide fuel cells. *ChemSusChem* **9**, 2443–2450 (2016).
26. Y. Liu, X. Zhu, M. Li, H. Liu, Y. Cong, W. Yang, Stabilization of low-temperature degradation in mixed ionic and electronic conducting perovskite oxygen permeation membranes. *Angew. Chem. Int. Ed.* **52**, 3232–3236 (2013).
27. H. Kwon, W. Lee, J. W. Han, Suppressing cation segregation on lanthanum-based perovskite oxides to enhance the stability of solid oxide fuel cell cathodes. *RSC Adv.* **6**, 69782–69789 (2016).
28. W. Lee, J. W. Han, Y. Chen, Z. Cai, B. Yildiz, Cation size mismatch and charge interactions drive dopant segregation at the surfaces of manganite perovskites. *J. Am. Chem. Soc.* **135**, 7909–7925 (2013).
29. T. Hong, F. Chen, C. Xia, Barium carbonate nanoparticle to enhance oxygen reduction activity of strontium doped lanthanum ferrite for solid oxide fuel cell. *J. Power Sources* **278**, 741–750 (2015).
30. J. Gao, Y. Meng, S. Lee, J. Tong, K. S. Brinkman, Effect of infiltration of barium carbonate nanoparticles on the electrochemical performance of $La_{0.6}Sr_{0.4}Co_{0.2}Fe_{0.8}O_{3-\delta}$ cathodes for protonic ceramic fuel cells. *JOM* **71**, 90–95 (2018).
31. Z. Shao, W. Yang, Y. Cong, H. Dong, J. Tong, G. Xiong, Investigation of the permeation behavior and stability of a $Ba_{0.5}Sr_{0.5}Co_{0.8}Fe_{0.2}O_{3-\delta}$ oxygen membrane. *J. Membr. Sci.* **172**, 177–188 (2000).
32. J. F. Shin, W. Xu, M. Zanella, K. Dawson, S. N. Savvin, J. B. Claridge, M. J. Rosseinsky, Self-assembled dynamic perovskite composite cathodes for intermediate temperature solid oxide fuel cells. *Nat. Energy* **2**, 16214 (2017).
33. G. Chen, W. Zhou, D. Guan, J. Sunarso, Y. Zhu, X. Hu, W. Zhang, Z. Shao, Two orders of magnitude enhancement in oxygen evolution reactivity on amorphous $Ba_{0.5}Sr_{0.5}Co_{0.8}Fe_{0.2}O_{3-\delta}$ nanofilms with tunable oxidation state. *Sci. Adv.* **3**, e1603206 (2017).
34. Y. A. Mastrikov, M. M. Kuklja, E. A. Kotomin, J. Maier, First-principles modelling of complex perovskite $(Ba_{1-x}Sr_x)(Co_{1-y}Fe_y)O_{3-\delta}$ for solid oxide fuel cell and gas separation membrane applications. *Energy Environ. Sci.* **3**, 1544–1550 (2010).
35. T. Jung, J. G. Na, D. W. Cho, J. H. Park, R. T. Yang, $Ba_xSr_{1-x}O$/MgO nano-composite sorbents for tuning the transition pressure of oxygen: Application to air separation. *Chem. Eng. Sci.* **137**, 532–540 (2015).
36. X. Chen, T. Jung, J. Park, W. S. Kim, Preparation of single-phase three-component alkaline earth oxide of (BaSrMg)O: A high capacity and thermally stable chemisorbent for oxygen separation. *J. Mater. Chem. A* **3**, 258–265 (2015).
37. Y. Zhu, W. Li, Y. Liu, X. Zhu, W. Yang, Selection of oxygen permeation models for different mixed ionic-electronic conducting membranes. *AIChE J.* **63**, 4043–4053 (2017).
38. J. Lu, C. Zhu, C. Pan, W. Lin, J. P. Lemmon, F. Chen, C. Li, K. Xie, Highly efficient electrochemical reforming of CH_4/CO_2 in a solid oxide electrolyser. *Sci. Adv.* **4**, eaar5100 (2018).
39. J. H. Park, Y. Kwon, G. D. Nam, J. H. Joo, Simultaneous conversion of carbon dioxide and methane to syngas using an oxygen transport membrane in pure CO_2 and CH_4 atmospheres. *J. Mater. Chem. A* **6**, 14246–14254 (2018).
40. P. W. Tasker, The stability of ionic crystal surfaces. *J. Phys. C Solid State Phys.* **12**, 4977–4984 (1979).
41. P. D. VerNooy, Redetermination of the structure of barium peroxide by single-crystal x-ray diffraction. *Acta Crystallogr. C* **49**, 433–434 (1993).
42. A. K. Huber, M. Falk, M. Rohnke, B. Luerßen, L. Gregoratti, M. Amati, J. Janek, In situ study of electrochemical activation and surface segregation of the SOFC electrode material $La_{0.75}Sr_{0.25}Cr_{0.5}Mn_{0.5}O_{3\pm\delta}$. *Phys. Chem. Chem. Phys.* **14**, 751–758 (2012).
43. A. K. Huber, M. Falk, M. Rohnke, B. Luerssen, M. Amati, L. Gregoratti, D. Hesse, J. Janek, In situ study of activation and de-activation of LSM fuel cell cathodes—Electrochemistry and surface analysis of thin-film electrodes. *J. Catal.* **294**, 79–88 (2012).
44. G. Kresse, J. Furthmüller, Efficiency of ab-initio total energy calculations for metals and semiconductors using a plane-wave basis set. *Comp. Mater. Sci.* **6**, 15–50 (1996).
45. G. Kresse, J. Furthmüller, Efficient iterative schemes for ab initio total-energy calculations using a plane-wave basis set. *Phys. Rev. B Condens Matter* **54**, 11169–11186 (1996).
46. P. E. Blöchl, Projector augmented-wave method. *Phys. Rev. B* **50**, 17953–17979 (1994).
47. J. P. Perdew, Y. Wang, Accurate and simple analytic representation of the electron-gas correlation energy. *Phys. Rev. B* **45**, 13244–13249 (1992).
48. S. Grimme, Semiempirical GGA-type density functional constructed with a long-range dispersion correction. *J. Comput. Chem.* **27**, 1787–1799 (2006).
49. S. Kirklin, J. E. Saal, B. Meredig, A. Thompson, J. W. Doak, M. Aykol, S. Rühl, C. Wolverton, The Open Quantum Materials Database (OQMD): Assessing the accuracy of DFT formation energies. *NPJ Comput. Mater.* **1**, 15010 (2015).
50. N. Han, Y. Wang, H. Yang, J. Deng, J. Wu, Y. Li, Y. Li, Ultrathin bismuth nanosheets from in situ topotactic transformation for selective electrocatalytic CO_2 reduction to formate. *Nat. Commun.* **9**, 1320 (2018).
51. L. Zhang, W. Long, F. Jin, T. He, Electrical conductivity, thermal expansion and electrochemical performances of Ba-doped $SrCo_{0.9}Nb_{0.1}O_{3-\delta}$ cathodes for IT-SOFCs. *Int. J. Hydrogen Energy* **38**, 7947–7956 (2013).
52. J. Peña-Martínez, D. Marrero-López, D. Pérez-Coll, J. C. Ruiz-Morales, P. Núñez, Performance of XSCoF (X=Ba, La and Sm) and LSCrX′ (X′=Mn, Fe and Al) perovskite-structure materials on LSGM electrolyte for IT-SOFC. *Electrochim. Acta* **52**, 2950–2958 (2007).
53. O. Celikbilek, C. A. Thieu, F. Agnese, E. Cali, C. Lenser, N. H. Menzler, J. W. Son, S. J. Skinner, E. Djurado, Enhanced catalytic activity of nanostructured, A-site deficient $(La_{0.7}Sr_{0.3})_{0.95}(Co_{0.2}Fe_{0.8})O_{3-\delta}$ for SOFC cathodes. *J. Mater. Chem. A* **7**, 25102–25111 (2019).
54. E. Lee, Y. Lim, E. A. Lee, H. J. Hwang, J. W. Moon, $Ba_{0.5}Sr_{0.5}Co_{0.8}Fe_{0.2}O_{3-\delta}$ (BSCF) and $La_{0.6}Ba_{0.4}Co_{0.2}Fe_{0.8}O_{3-\delta}$ (LBCF) cathodes prepared by combined citrate-EDTA method for IT-SOFCs. *J. Power Sources* **157**, 848–854 (2006).
55. Y.-J. Choe, H.-J. Hwang, Electrochemical performance and Cr tolerance in a $La_{1-x}Ba_xCo_{0.9}Fe_{0.1}O_{3-\delta}$ (x = 0.3, 0.4 and 0.5) cathode for solid oxide fuel cells. *J. Korean Ceram. Soc.* **52**, 308–314 (2015).
56. J. Gao, X. Song, F. Zhou, S. An, Y. Tian, Substituent effects of Ba^{2+} for Sm^{3+} on the structure and electrochemical performances of $Sm_{0.5}Sr_{0.5}Co_{0.8}Fe_{0.2}O_{3-\delta}$ cathode for intermediate temperature solid oxide fuel cells. *J. Power Sources* **218**, 383–392 (2012).
57. S. Sydyknazar, V. Cascos, L. Troncoso, A. L. Larralde, M. T. Fernandez-Diaz, J. A. Alonso, Design, synthesis, structure and properties of Ba-doped derivatives of $SrCo_{0.95}Ru_{0.05}O_{3-\delta}$ perovskite as cathode materials for SOFCs. *Materials* **12**, 1957 (2019).
58. X. Zhu, H. Liu, Y. Cong, W. Yang, Permeation model and experimental investigation of mixed conducting membranes. *AIChE J.* **58**, 1744–1754 (2012).
59. D. Oh, D. Gostovic, E. Wachsman, Mechanism of $La_{0.6}Sr_{0.4}Co_{0.2}Fe_{0.8}O_{3-\delta}$ cathode degradation. *J. Mater. Res.* **27**, 1992–1999 (2012).
60. X. Zhu, H. Wang, W. Yang, Structural stability and oxygen permeability of cerium lightlydoped $BaFeO_{3-\delta}$ ceramic membranes. *Solid state Ionics* **177**, 2917–2921 (2006).
61. G. Mestl, M. P. Rosynek, J. H. Lunsford, Decomposition of nitric oxide over barium oxide supported on magnesium oxide. 4. In situ Raman characterization of oxide phase transitions and peroxide species by ^{18}O-labeling. *J. Phys. Chem. B* **102**, 154–161 (1998).
62. G. Mestl, M. P. Rosynek, J. H. Lunsford, Decomposition of nitric oxide over barium oxide supported on magnesium oxide. 3. In situ Raman characterization of the role of oxygen. *J. Phys. Chem. B* **101**, 9329–9334 (1997).
63. S. Xie, J. H. Lunsford, A catalytic and in situ raman spectroscopy study of the decomposition of nitrous oxide over barium oxide supported on magnesium oxide. *Appl. Catal. A Gen.* **188**, 137–144 (1999).
64. R. P. Stoffel, R. Dronskowski, Barium peroxide: A simple test case for first-principles investigations on the temperature dependence of solid-state vibrational frequencies. *Z. Anorg. Allg. Chem.* **638**, 1403–1406 (2012).
65. S. Xie, P. R. Michael, J. H. Lunsford, Effect of laser heating on the local temperature and composition in Raman spectroscopy: A study of $Ba(NO_3)_2$ and BaO_2 decomposition. *Appl. Spectrosc.* **53**, 1183–1187 (1999).
66. S. C. Su, A. T. Bell, Raman studies of peroxide formation, decomposition, and reduction on Ba/MgO. *Catal. Lett.* **36**, 15–19 (1996).
67. J. H. Lunsford, X. Yang, K. Haller, J. Laane, In situ Raman spectroscopy of peroxide ions on barium/magnesium oxide catalysts. *J. Phys. Chem. B* **97**, 13810–13813 (1993).

68. K. Haller, J. H. Lunsford, J. Laane, Temperature dependence of the Raman spectrum of barium peroxide. *J. Phys. Chem. B* **100**, 551–555 (1996).
69. A. Sacuto, D. Colson, A. Forget, J. Cayssol, Raman scattering on oxide phases related to the mercurate high-Tc superconductors. *Phys. C* **341-348**, 2253–2254 (2000).
70. D. Waal, K.-J. Range, M. Konigstein, W. Kiefer, Raman spectra of the barium oxide peroxide and strontium oxide peroxide series. *J. Raman Spectrosc.* **29**, 109–113 (1998).
71. M. Konigstein, Structural properties of nonstoichiometric barium and strontium peroxides: BaO_{2-x}(1.972-x1.72) and SrO_{2-x}(1.982-x1.90). *J. Solid State Chem.* **147**, 478–484 (1999).
72. Y. Che, Y. Choi, S. Yoo, Y. Ding, R. Yan, K. Pei, C. Qu, L. Zhang, I. Chang, B. Zhao, Y. Zhang, H. Chen, Y. Chen, C. Yang, B. deGlee, R. Murphy, J. Liu, M. Liu, A highly efficient multi-phase catalyst dramatically enhances the rate of oxygen reduction. *Joule* **2**, 938–949 (2018).
73. W. Fan, Z. Sun, J. Wang, J. Zhou, K. Wu, Y. Cheng, Evaluation of $Sm_{0.95}Ba_{0.05}Fe_{0.95}Ru_{0.05}O_3$ as a potential cathode material for solid oxide fuel cells. *RSC Adv.* **6**, 34564–34573 (2016).
74. X. Yu, C. Sui, R. Ren, J. Qiao, W. Sun, Z. Wang, K. Sun, Construction of heterointerfaces with enhanced oxygen reduction kinetics for intermediate-temperature solid oxide fuel cells. *ACS Appl. Energy Mater.* **3**, 447–455 (2020).
75. H.-N. Im, M.-B. Choi, B. Singh, D.-K. Lim, S.-J. Songz, Investigation of oxygen reduction reaction on $La_{0.1}Sr_{0.9}Co_{0.8}Fe_{0.2}O_{3-\delta}$ electrode by electrochemical impedance spectroscopy. *J. Electrochem. Soc.* **162**, F728–F735 (2015).
76. J. Wang, L. Jiang, X. Xiong, C. Zhang, X. Jin, L. Lei, K. Huang, A broad stability investigation of Nb-Doped $SrCoO_{2.5+\delta}$ as a reversible oxygen electrode for intermediate-temperature solid oxide fuel cells. *J. Electrochem. Soc.* **163**, F891–F898 (2016).

Acknowledgments: We acknowledge the assistance of T. Yang and C. Wang from the Division of Energy Research Resources of Dalian National Laboratory for Clean Energy on XRD and TG. We also acknowledge the assistance of N. Ta and X. Wei from the State Key Laboratory of Catalysis of Dalian Institute of Chemical Physics on SEM and HRSEM. **Funding:** This work was supported by Strategic Priority Research Program of the Chinese Academy of Sciences (grant no. XDB17000000), Youth Innovation Promotion Association of CAS (Y201829), the National Natural Science Foundation of China (grant nos. 22072150 and 22178332), and the China Postdoctoral Science Foundation (grant no. 2021M693131).
Author contributions: Conceptualization: Y. Zhu, X. Zhu and W. Yang; Methodology: Y. Zhu, X. Zhu, W. Yang, D. Liu, H. Jing, W. Liu, J. Xiao and F. Fan; Investigation: Y. Zhu, D. Liu, H. Jing, F. Zhang, S. Hu, L. Zhang and J. Wang; Visualization: Y. Zhu, D. Liu, H. Jing, X. Zhang, L. Zhang, W. Zhang, B. Pang and P. Zhang; Supervision: W. Yang, X. Zhu, W. Liu and J. Xiao; Writing – original draft: Y. Zhu, H. Jing and X. Zhu; Writing – review & editing: Y. Zhu, X. Zhu, W. Yang, H. Jing, J. Xiao and W. Liu. **Competing interests:** The authors declare that they have no competing interests. **Data and materials availability:** All data needed to evaluate the conclusions in the paper are present in the paper and/or the Supplementary Materials.

Submitted 24 November 2021
Accepted 22 February 2022
Published 13 April 2022
10.1126/sciadv.abn4072